(Preprint) AAS 23-126

AUTONOMOUS ONBOARD RISK MITIGATION FOR SPACECRAFT PROXIMITY OPERATIONS; A ZERO-SWAP FLIGHT SOFTWARE ENHANCEMENT

Benjamin Sunderland[*], Shota Takahashi[†], Siamak Hesar[‡], Axel Garcia[§], Mark Muktoyuk[¶], Rachel Mamich[‖], Renato Zanetti[**], and Moriba Jah[††]

Advanced rendezvous proximity operations (RPO) and docking (RPOD) capabilities are essential for ensuring sustainable growth in the commercial space industry. These capabilities open the door to performing complex operations including spacecraft-to-spacecraft inspection, in-situ tracking, active debris removal, refueling, and on-orbit manufacturing. Traditional operations solutions are extremely manual with ground-in-the-loop processes for orchestrating maneuver planning, asset tracking, and performing corrective actions. Autonomous processes are required to ensure efficiency, timeliness, and scalability of such missions. In this paper, we demonstrate the development of a practical and computationally efficient zero-SWaP flight software (FSW) enhancement to enable safe and autonomous proximity operations (ProxOps) between a servicer spacecraft and resident space object (RSO). This is achieved via a system-agnostic module that continuously receives information from the orbit determination and relative navigation filters and autonomously computes relative orbit formation reconfiguration maneuvers, optimized to minimize fuel expenditure and evaluated for spacecraft safety. A nominal ProxOps use case is developed and simulation results illustrate the performance of these algorithms in terms of the required ΔV, associated risk of the transfer trajectory, and the accuracy of the relative motion dynamics model. Recommendations are made for further improvements to the state model representation, dynamics model fidelity, and the overall risk characterization and mitigation strategy.

INTRODUCTION

A zero-SWaP FSW enhancement is proposed that does not require costly state-of-the-art sensor suites or ADCS hardware additions and that is compatible with systems that have low power and processing capabilities. These are all common design limitations for commercial satellites of today that increasingly use small form factors and standardized buses. The central focus of this effort is providing a servicer spacecraft with the ability to perform RPO and RPOD activities autonomously. This will reduce the cost and latency associated with ground communications and enable the servicer to respond to changes in its environment more quickly; the safety margin required in preparation for communication loss will also be minimized. Additionally, there are many sources of uncertainty in the state knowledge of the servicer and RSO due to orbit determination errors which must be taken into consideration; these uncertainties evolve over time due to unmodeled dynamics, uncertain model parameters, and maneuvers of the servicing spacecraft that introduce noise in the state. Thus, the servicing spacecraft needs to account for these uncertainties and perform trajectory planning to ensure operational safety. This paper demonstrates how these criteria can be achieved

[*]Sr. Astrodynamics Engineer, Kayhan Space, 1460 Overlook Dr, Lafayette, CO 80026.
[†]Sr. Astrodynamics Engineer, Kayhan Space, 1460 Overlook Dr, Lafayette, CO 80026.
[‡]Chief Executive Officer, Kayhan Space, 1460 Overlook Dr, Lafayette, CO 80026.
[§]GNC Engineer, Astroscale U.S., 2201 S Delaware St, Denver, CO 80223.
[¶]Senior GNC Systems Engineer, Astroscale U.S., 2201 S Delaware St, Denver, CO 80223.
[‖]PhD Student, Aerospace Engineering and Engineering Mechanics, UT Austin, 2617 Wichita St, Austin, TX 78712.
[**]Assistant Professor, Aerospace Engineering and Engineering Mechanics, UT Austin, 2617 Wichita St, Austin, TX 78712.
[††]Associate Professor, Aerospace Engineering and Engineering Mechanics, UT Austin, 2617 Wichita St, Austin, TX 78712.

via an onboard software capability that continuously receives information from the orbit determination and relative navigation filters and autonomously computes relative orbit formation reconfiguration maneuvers, optimized for fuel expenditure and evaluated for spacecraft safety. Kayhan Space is developing this zero-SWaP FSW enhancement as Kaynan Proxima in cooperation with Astroscale US and the University of Texas at Austin. A notional GN&C system diagram including the FSW enhancement by Kayhan Proxima for autonomous path planning is shown in Figure **??**.

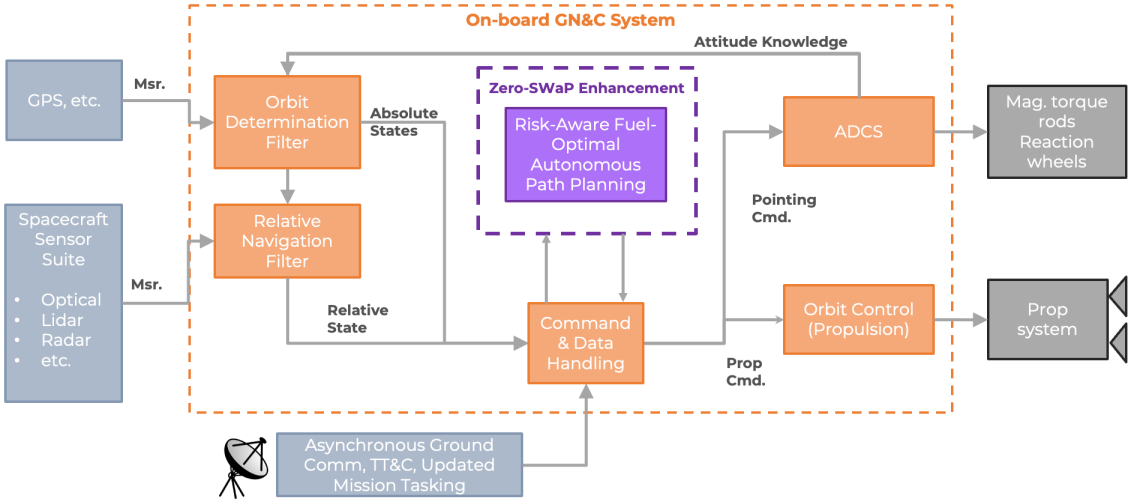

Figure 1: Notional System Diagram for On-Board GN&C System.

A diagram of the proposed process for the autonomous path planning algorithm is shown in Figure **??**, where the central control policy is based on the n-impulse fuel-optimal maneuver targeting algorithm designed by Roscoe, et al. that formed the basis of the formation reconfiguration guidance component for NASA's CubeSat proximity operations demonstration (CPOD) mission.[?,?] This approach was chosen for its benefits of minimizing fuel consumption thereby enabling servicer spacecraft to potentially extend their missions; it also exclusively employs linear systems for the formation dynamics and the solution to the optimal control problem (OCP), making it computationally efficient and suitable for on-board FSW.

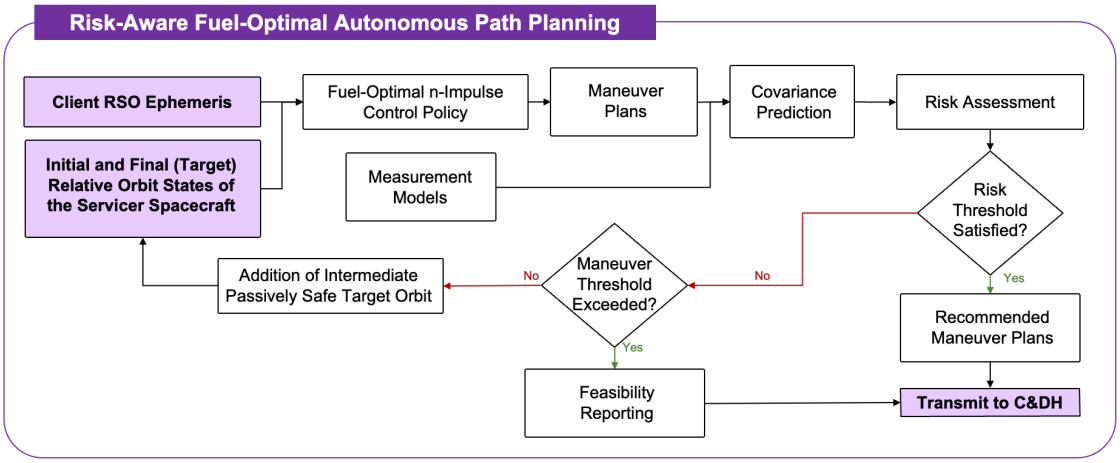

Figure 2: Notional Risk-Aware Fuel-Optimal Autonomous Path Planning Flow Chart.

This paper is divided into two major sections for methodology and results, where the following methodology sections explore different representations of the relative state between a servicer spacecraft and client RSO; the relative formation dynamics; the proposed autonomous path planning algorithms including risk assessment and quantification, as well as; the development of an analytical guidance law for computing trajectory correction maneuvers (TCMs) to keep the servicer spacecraft on the nominal planned path. A ProxOps use case is developed where the servicer spacecraft starts in an initial formation with the client RSO and targets the necessary impulsive maneuvers to bring it to a new relative formation at a specified time. The ability of the autonomous path-planning algorithm to achieve a fuel-optimal formation reconfiguration while accounting for spacecraft safety is demonstrated via numerical simulation for the nominal use case. A risk analysis and subsequent dispersion analysis are conducted to evaluate the safety of the trajectory generated by the control policy. The cumulative error in the relative position of the servicer spacecraft due to unmodeled perturbations in the analytical dynamics model is quantified by propagating the nominal scenario with numerical integration of higher fidelity equations of motion. The ability of the aforementioned analytical guidance law for TCMs to correct for such errors is then demonstrated. Finally, the control commands from the proposed autonomous path planning policy are evaluated by Astroscale using a higher-fidelity 6-DOF simulator.

PROBLEM STATEMENT

Formation Design

The most common parameterization for the relative motion of two spacecraft uses relative Cartesian coordinates in the Hill frame $\mathcal{H} : \{\hat{\boldsymbol{h}}_1, \hat{\boldsymbol{h}}_2, \hat{\boldsymbol{h}}_3\}$ as shown in Figure **??**. This is a rotating frame based on the reference orbit of the RSO where $\hat{\boldsymbol{h}}_1$ is the unit vector pointing in the direction of the RSO's position, $\hat{\boldsymbol{h}}_3$ is the orbit-normal unit vector in the direction of the RSO's angular momentum vector, and $\hat{\boldsymbol{h}}_2 = \hat{\boldsymbol{h}}_3 \times \hat{\boldsymbol{h}}_1$ completes the right-handed system. The relative position vector of the servicer is defined by $\boldsymbol{\rho} = (x, y, z)^T$ with the relative velocity $\dot{\boldsymbol{\rho}} \triangleq {}^{\mathcal{H}}d\boldsymbol{\rho}/dt = (\dot{x}, \dot{y}, \dot{z})^T$, where ${}^{\mathcal{H}}d(\cdot)/dt$ denotes the time derivative taken in the rotating reference frame and the 6-dimensional relative Cartesian state vector is $\delta\boldsymbol{x} = (\boldsymbol{\rho}, \dot{\boldsymbol{\rho}})^T$.

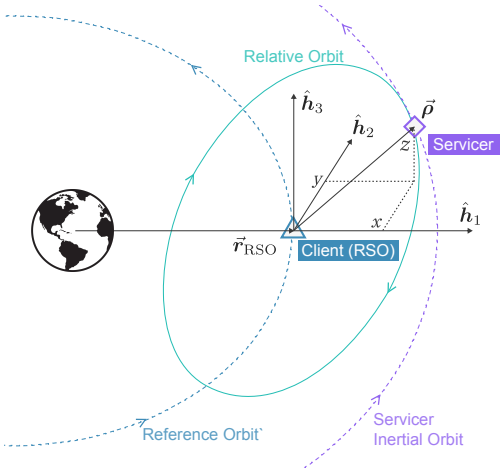

Figure 3: Illustration of a General Spacecraft Formation with Out-of-Plane Relative Motion.

The second most common parameterization used for formation design and modeling relative spacecraft dynamics is that of differential orbital elements, or simply the arithmetic difference between the servicer and reference orbital elements: $\delta\boldsymbol{oe} = \boldsymbol{oe}_{\mathrm{Servicer}} - \boldsymbol{oe}_{\mathrm{RSO}}$. This state representation is particularly useful for spacecraft dynamics modeling in general due to the absolute orbital elements' slow rate of change, limited to the mean anomaly M or true anomaly f for unperturbed Keplerian motion, as compared to the relative Cartesian representation which is composed of six so-called "fast variables".[?] This paper will use the nearly non-singular set of orbital elements: $\boldsymbol{oe}_{\mathrm{nns}} = (a, \lambda, i, q_1, q_2, \Omega)^T$ where a is the semimajor axis, $\lambda = M + \omega$ is the mean argument of latitude, ω is the argument of perigee, i is the orbit inclination, $q_1 \equiv e_x = e\cos\omega$

and $q_2 \equiv e_y = e\sin\omega$ are the eccentricity vector components, e is the orbit eccentricity, and Ω is the right ascension of the ascending node. Although the work presented here will be broadly applicable with any $\boldsymbol{oe}$-based state representation, this particular one was chosen for its benefits of avoiding the singularity for the undefined line of apsides (when $e = 0$) as well as being extensively used throughout other bodies of work in the realm of relative spacecraft dynamics (sometimes with the true argument of latitude, $\theta = f + \omega$, instead).[?,?]

Formation Dynamics

This study leveraged the analytic solution for relative formation dynamics developed by Gim and Alfriend,[?] henceforth referred to as the "GA Method", accommodating for an eccentric reference orbit and J_2 perturbation effects based on Brouwer's solution.[?] While Brouwer's solution captures second-order secular and first-order periodic perturbations about a Keplerian reference orbit due to $J_2 - J_5$, the GA Method retains only the first-order secular J_2 terms. Gim and Alfriend utilize the Lagrange planetary equations (LPEs), defining the orbital element variations due to first-order J_2 effects, and derive the analytical state transition matrix (GA STM) for differential nearly non-singular *mean* orbital elements:

$$\delta\bar{\boldsymbol{oe}}_{\text{nns}}(t) = \bar{\boldsymbol{\phi}}_{J_2}(t, t_0)\delta\bar{\boldsymbol{oe}}_{\text{nns}}(t_0) \tag{1}$$

where $\delta\bar{\boldsymbol{oe}}_{\text{nns}} = (\delta\bar{a}, \delta\bar{\lambda}, \delta\bar{i}, \delta\bar{q_1}, \delta\bar{q_2}, \delta\bar{\Omega})^T$ represents the set of differential nearly-nonsingular mean orbital elements of the servicer spacecraft with respect to the reference orbit. Note that ($\bar{}$) and ($\tilde{}$) are used to distinguish between *mean* and *osculating* orbital elements, respectively. In order to employ Equation (**??**) to propagate the osculating relative Cartesian state in the Hill frame and the corresponding state-covariance, a number of additional transformations are necessary. A summary of the full derivation is provided below for reference, but the reader is referred to the original work of Gim and Alfriend for full detail.[?]

The non-linear transformation between mean and osculating absolute orbital elements is given by:

$$\widetilde{\boldsymbol{oe}}_{\text{nns}} = \bar{\boldsymbol{oe}}_{\text{nns}} - (J_2 R_e^2)\{\Delta\boldsymbol{oe}^{(lp)}_{\text{nns}} + \Delta\boldsymbol{oe}^{(sp1)}_{\text{nns}} + \Delta\boldsymbol{oe}^{(sp2)}_{\text{nns}}\} \tag{2}$$

where $\Delta\boldsymbol{oe}^{(lp)}_{\text{nns}}$ is a function of the long-periodic generating function, then $\Delta\boldsymbol{oe}^{(sp1)}_{\text{nns}}$ and $\Delta\boldsymbol{oe}^{(sp2)}_{\text{nns}}$ are component functions of the short-periodic generating function. Similarly, the linearized mapping between mean and osculating differential orbital elements is found by computing the Jacobian, $D(\delta\bar{\boldsymbol{oe}}_{\text{nns}}(t))$:

$$D(t) = \frac{\delta\widetilde{\boldsymbol{oe}}_{\text{nns}}}{\delta\bar{\boldsymbol{oe}}_{\text{nns}}} = I - (J_2 R_e^2)[D^{(lp)}(t) + D^{(sp1)}(t) + D^{(sp2)}(t)] \tag{3}$$

The linear mapping matrix for the geometric transformation between differential osculating orbital elements and relative Cartesian Hill frame coordinates, $\Sigma(\widetilde{\boldsymbol{oe}}_{\text{nns}}(t))$, is given by:

$$\Sigma(t) = \{A(t) + \alpha B(t)\} \tag{4}$$

where $A(t)$ is the unperturbed linear mapping, $B(t)$ captures frame rotation rate effect caused by J_2, $\alpha = 3J_2R_e^2$, and $\delta\boldsymbol{x}(t) = \Sigma(t) \times \delta\widetilde{\boldsymbol{oe}}_{\text{nns}}(t)$. The full GA STM for propagating the osculating relative Cartesian state in Hill Frame coordinates is thus given by combining Equations (**??**), (**??**), and (**??**):

$$\Phi_{J_2}(t, t_0) = \{A(t) + \alpha B(t)\}D(t)\bar{\boldsymbol{\phi}}_{J_2}(t, t_0)D^{-1}(t_0)\{A(t_0) + \alpha B(t_0)\}^{-1} \tag{5}$$

The analytical solution for $\Sigma^{-1}(t)$ is additionally included in the GA Method, and the first-order approximate inverse of Equations (**??**)−(**??**) can be obtained by replacing J_2 with $-J_2$ and treating the osculating elements as the inputs to the Brouwer transformation.[?] Finally, for the purposes of this paper, Equations (**??**)−(**??**) were modified to use the mean argument of latitude, λ, instead of the true argument of latitude, θ.

In order to include the control influence, $\boldsymbol{u}$, on the differential mean orbital elements it can be shown that:

$$\delta\bar{\boldsymbol{oe}}_{\text{nns}}(t) = \bar{\boldsymbol{\phi}}_{J_2}(t, t_0)\delta\bar{\boldsymbol{oe}}_{\text{nns}}(t_0) + \int_{t_0}^{t} \bar{\boldsymbol{\phi}}_{J_2}(t, \tau)B(\tau)\boldsymbol{u}(\tau)d\tau \tag{6}$$

where $B(t)$ represents Gauss's variational equations (GVEs) evaluated on the reference orbit.[?]

It is useful to note that, while this form of the GA Method was used for the analyses throughout this paper, there exist many alternative differential orbital elements-based formulations of the relative motion dynamics throughout literature. Two such variations of the GA method include the small-eccentricity version of (**??**)−(**??**) which can be used to save significant computational effort for formations in near-circular reference orbits, given by Alfriend and Yan,[?] and; the GA Method using differential equinoctial elements which avoids singularities for both the line of apsides being undefined (when $e = 0$) and the line of nodes being undefined (when $i = 0$).[?] The following sections will show how Equation (**??**) is used to capture the formation dynamics during the control policy portion of the autonomous path planning algorithms, and the full GA STM from Equation (**??**) is used to propagate the Hill frame relative Cartesian state-covariance for risk assessment.

Autonomous Path Planning

The aforementioned fuel-optimal maneuver targeting algorithm designed by Roscoe, et al. was developed to iteratively solve the *n*-impulse maneuver targeting problem, formulated as a discrete-time OCP while using Laweden's primer vector theory[?] to improve the resulting sub-optimal set of impulses until they converge to the optimal values using the necessary conditions of the corresponding continuous-time OCP formulation. A flowchart of the algorithm is shown in Figure **??** where the discrete-time OCP is initially solved for a large number of impulses (e.g. 24 per orbit period), the times corresponding to the local maxima in the resulting impulse history are then chosen as the candidate optimal maneuver times, and the suboptimal trajectory is then incrementally improved by moving, adding, or removing the impulses based off of the primer vector magnitude history; the reader is referred to the original work of Roscoe et al for full detail.[?]

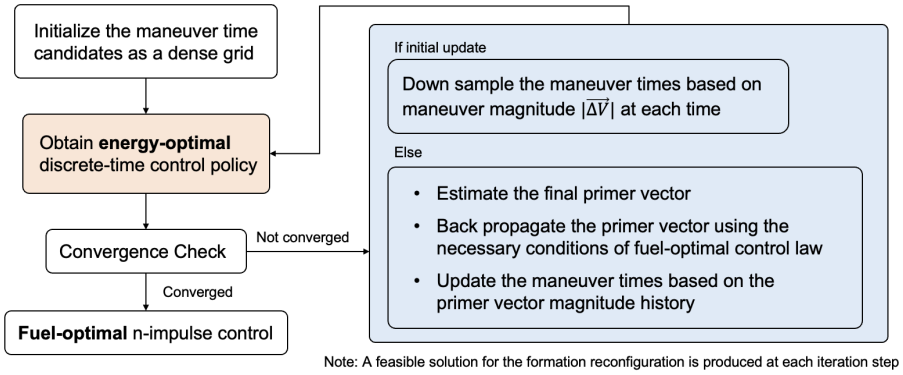

Figure 4: Flow Diagram of the Fuel-Optimal N-Impulse Transfer Design

This process uses the core GA-STM for differential mean orbital elements and the control effect is incorporated using GVEs (Equations (**??**) and (**??**)). Once the nominal fuel-optimal maneuver plan has been solved, the relative state-covariance of the servicer is subsequently propagated using the *full* GA-STM from Equation (**??**) for the purpose of propagating the relative Cartesian state-covariance and quantifying the risk associated with the nominal maneuver plan (see Figure **??**). If the pre-defined risk threshold criteria are satisfied, the recommended maneuver plan is transmitted to the C&DH interface; otherwise, an intermediate passively safe transfer orbit can be additionally targeted to reduce risk in the transfer trajectory.

The path planning algorithm is designed to take the initial states of both the client RSO and the servicer spacecraft along with the final targeted relative orbit state for the servicer spacecraft. It is anticipated that flight systems will have broadly varying native representations for absolute and relative states; therefore, this interface was made to generically handle conversions of absolute states to mean orbital elements and relative states to differential mean orbital elements through the appropriate nonlinear transformation processes.

Risk Assessment and Quantification

For safe and autonomous spacecraft servicing, the guidance algorithm needs to be cognizant of future high-risk events. In the following sections, the approaches taken to assess the collisional risk between the client and servicer spacecraft are described.

Covariance Prediction The most fundamental information for the collision risk is the covariance of the client's and servicer's state uncertainties. This study focuses on the relative state covariance and does not consider individual covariances of the two objects for risk assessment purposes.

Based on the latest navigation solution, the client spacecraft must evaluate the risks associated with the predicted future relative trajectory. When no measurements are taken, the covariance evolves according to the dynamics. The Hill frame relative state covariance propagated by the natural dynamics is

$$\begin{aligned} P(t) &\equiv E\left[(\boldsymbol{x}(t)-\bar{\boldsymbol{x}}(t))^T(\boldsymbol{x}(t)-\bar{\boldsymbol{x}}(t))\right] \\ &= \Phi_{J2}(t,t_0)\cdot P(t_0)\cdot\Phi_{J2}^T(t,t_0) \end{aligned} \tag{7}$$

where E is the expectation operator, $\boldsymbol{x}=(\boldsymbol{\rho},\dot{\boldsymbol{\rho}})^T$ is the Hill frame relative state, $\bar{\boldsymbol{x}}$ is its mean, and $\Phi_{J2}=\partial\boldsymbol{x}(t)/\partial\boldsymbol{x}(t_0)$ is the linear mapping between the relative states through GA-STM.

The Gates' maneuver uncertainty model[?] is employed in this study to account for the servicer spacecraft's maneuver execution noise. At the time of an impulsive maneuver, the following maneuver covariance is added.

$$P_{\boldsymbol{\Delta V}}=[\sigma_s^2(\Delta V)^2+\sigma_r^2]\hat{\boldsymbol{v}}\hat{\boldsymbol{v}}+[\sigma_p^2(\Delta V)^2+\sigma_a^2](I-\hat{\boldsymbol{v}}\hat{\boldsymbol{v}}) \tag{8}$$

where $\hat{\boldsymbol{v}}=\boldsymbol{\Delta V}/|\boldsymbol{\Delta V}|$.

With the natural dynamics, the covariance grows over time, especially the in-track component. During RPO, it is reasonable to assume that the servicer spacecraft has constant access to the navigation solutions. Thus, it is practical to make covariance predictions assuming some measurement updates.

The relative position bearing angle measurement by optical sensors and range measurements are considered.

$$\boldsymbol{Y}_{\text{optical}}=\left[\arctan\left(y/x\right),\arctan\left(z/\sqrt{x^2+y^2}\right)\right] \tag{9}$$

$$Y_{\text{range}}=|\boldsymbol{\rho}| \tag{10}$$

where x, y, and z are Hill frame components of the relative position vector $\boldsymbol{\rho}$. The measurement models have corresponding noise covariance R. The contribution of the future measurements on the covariance is incorporated by assuming that the measurements are taken at the maximum likelihood state, linearizing the measurement models. The Joseph formulation of the Kalman filter covariance update equations is used.[?]

$$P_k=(I-K_k\cdot\tilde{H}_k)\cdot\bar{P}_k\cdot(I-K_k\tilde{H}_k)^T+K_k\cdot R_k\cdot K_k^T \tag{11}$$

$$K_k=\bar{P}_k\cdot\tilde{H}_k^T\cdot[\tilde{H}_k\cdot\bar{P}_k\cdot\tilde{H}_k^T+R_k]^{-1} \tag{12}$$

where the subscript k indicates k-th measurement update; $\bar{P}$ is the a priori covariance; $\tilde{H}$ is the measurement partial.

Finally, process noise must be included for the purpose of maintaining a realistic predicted covariance. The noise acceleration is assumed to be a piecewise constant white Gaussian sequence $\boldsymbol{u}(t_i)$ rather than a process.[?] The covariance propagation equation has an additional noise contribution.

$$\bar{P}_{k+1}=\Phi_{J2}(t_{k+1},t_k)\cdot P_k\cdot\Phi_{J2}^T(t_{k+1},t_k)+\Gamma(t_{k+1},t_k)\cdot Q_k\cdot\Gamma^T(t_{k+1},t_k) \tag{13}$$

where Q_i is the process noise covariance

$$E[\boldsymbol{u}(t_i)\boldsymbol{u}(t_j)]=Q_i\delta_{ij} \tag{14}$$

and Γ is the process noise transition matrix.

Risk Metrics For risk evaluation, the study uses three different metrics. The simplest metric is the miss distance or the norm of the relative position $\boldsymbol{\rho}$. Another useful distance metric is the Mahalanobis distance in position space $\sqrt{\boldsymbol{\rho} \cdot P_{\boldsymbol{\rho}\boldsymbol{\rho}}^{-1} \cdot \boldsymbol{\rho}}$ where $P_{\boldsymbol{\rho}\boldsymbol{\rho}}$ is the 3×3 relative position covariance; the Mahalanobis distance in position space is specifically relevant for gaining insight into the instantaneous collisional risks.

Another class of risk metrics is the probability of collision (PC). A two-dimensional (2D) PC is used where the three-dimensional Gaussian distribution of the relative position at the time of closest approach (TCA) is marginalized as a 2D Gaussian distribution on the encounter plane.[?,?] The encounter plane is a plane perpendicular to the relative velocity at TCA. Relative velocity in the rotating Hill frame is used to construct the encounter plane. The 2D PC is given by

$$p_c = \int_{A_{\mathrm{hb}}} \frac{1}{2\pi\sqrt{|P_{\boldsymbol{d}\boldsymbol{d}}|}} \exp\left(-\frac{1}{2}\boldsymbol{d} \cdot P_{\boldsymbol{d}\boldsymbol{d}}^{-1} \cdot \boldsymbol{d}\right) dA \tag{15}$$

where $\boldsymbol{d}$ and $P_{\boldsymbol{d}\boldsymbol{d}}$ are the relative position vector and its covariance mapped onto the encounter plane; A_{hb} is the area swept by the combined hard body radius. For the purposes of this analysis, a circular area with a predefined hard body radius R_{hb} is used. The 2D PC computes a total collision probability for an isolated encounter, assuming the relative velocity is high enough that the relative motion is rectilinear. Another assumption is that relative covariance remains constant during an encounter. In general, 2D PC provides accurate collision probabilities for low Earth orbit conjunctions due to their high relative velocities. For RPO trajectories, the relative velocities are much smaller. However, assuming constant access to accurate navigation solutions, the time the spacecraft takes to travel a $1-\sigma$ position uncertainty could still be small, which motivates the use of the 2D PC. Results will be shown for both an analytical 2D PC formulation by Chan[?] and a numerical 2D PC implementation by Foster.[?,?] By definition, 2D PC is only applicable at TCA. However, this study computes 2D PC at any given time as it provides some insight into the risk trend. 2D PC computed at a point different from TCA is equivalent to 2D PC where the relative motion is approximated as a rectilinear motion with the position and velocity at that instance of time. We note that validating the accuracy of the 2D PC for the RPO scenarios considered in this work as well as studying the application of more accurate PC algorithms such as 3D PC[?] will be the focus of future studies.

Analytical Guidance Law with QCQP

On top of the nominal maneuver plans, the servicer spacecraft may need to perform trajectory correction maneuvers (TCMs). The spacecraft's trajectory deviates from the planned nominal trajectory due to various errors such as navigation errors, maneuver execution noise, and unmodeled dynamical perturbations. Without proper trajectory control, the deviation keeps growing, which might result in a higher collisional risk or violation of the mission constraints considered for the nominal trajectory design.

For the onboard generation of TCMs, the direct optimization of nonlinear programming (NLP) with various non-convex cost and constraint functions by iterative NLP solvers is generally not practical due to limited computational resources for flight systems.

Analytical computation of an impulsive TCM is considered based on quadratically constrained quadratic programming (QCQP)[?] with a single constraint. The algorithm finds an impulsive maneuver to minimize the future state deviation with the maximum $\boldsymbol{\Delta V}$ magnitude constraint. The benefit of this QCQP-based formulation is that the global solution can be obtained in a polynomial time. Furthermore, the specific problem considered here can be solved analytically. The complete replanning of the transfer trajectory to the target trajectory using the *n*-impulse fuel optimal control introduced earlier is another feasible option. However, if the goal is to keep the spacecraft close to the nominal path, a simple impulsive control may be sufficient. If the nominal trajectory is designed considering various mission-specific constraints, generating a whole new nominal path may not be ideal. Besides, with the QCQP-based formulation, the maneuver magnitude can be constrained.

The TCM can be obtained by solving the following QCQP.

$$\min_{\boldsymbol{\Delta V}} \quad J = \frac{1}{\Delta t}\int_{\tau}^{\tau+\Delta t} (\boldsymbol{x}(t) - \boldsymbol{x}_n(t)) \cdot W \cdot (\boldsymbol{x}(t) - \boldsymbol{x}_n(t)) dt \tag{16}$$

$$\text{subject to} \quad \boldsymbol{\Delta V} \cdot \boldsymbol{\Delta V} - v_{\max}^2 \leq 0 \tag{17}$$

where $\boldsymbol{x} = [\boldsymbol{\rho}, \dot{\boldsymbol{\rho}}]$ is the predicted relative state after applying the TCM, $\boldsymbol{x}_n$ is the nominal relative state, $W > 0$ is a positive definite 6x6 weight matrix defined by a user, and $v_{\max}$ is the maximum allowed $\boldsymbol{\Delta V}$ magnitude. The cost function is the time average of the state deviation from $t = \tau$ through $t = \tau + \Delta t$, and it can be discretized as

$$J = 1/N \sum_{i}^{N} (\boldsymbol{x}(t_i) - \boldsymbol{x}_n(t_i)) \cdot W \cdot (\boldsymbol{x}(t_i) - \boldsymbol{x}_n(t_i)) \tag{18}$$

Using the time average of the state deviation as a cost function results in a more consistent behavior than simply targeting a single state. If a single point in the future is targeted, the resulting trajectory might have a small cost at that epoch, but the state deviation could be much larger at other points. This is because a single impulse cannot control the full six state elements independently; the algorithm generally results in a nonzero cost.

With the linearized relative motion using GA-STM, the state after applying the TCM can be given as

$$\boldsymbol{x}(t_i) = \boldsymbol{x}_0(t_i) + T_i \cdot \boldsymbol{\Delta V} \tag{19}$$

where T_i is a matrix that maps the velocity change to the change in the relative position and velocity. Thus, the problem can be written in the following form.

$$\min_{\boldsymbol{\Delta V}} \quad J = A_o \cdot \boldsymbol{\Delta V} + 2\boldsymbol{b}_o \cdot \boldsymbol{\Delta V} + c_o \tag{20}$$

$$\text{subject to} \quad \boldsymbol{\Delta V} \cdot \boldsymbol{\Delta V} - v_{\max}^2 \leq 0 \tag{21}$$

where

$$A_o = 1/N \sum_{i}^{N} T_i^T \cdot W \cdot T_i \tag{22}$$

$$\boldsymbol{b}_o = 1/N \sum_{i}^{N} (\boldsymbol{x}_0(t_i) - \boldsymbol{x}_n(t_i)) \cdot W \cdot T_i \tag{23}$$

$$c_o = 1/N \sum_{i}^{N} (\boldsymbol{x}_0(t_i) - \boldsymbol{x}_n(t_i)) \cdot W \cdot (\boldsymbol{x}_0(t_i) - \boldsymbol{x}_n(t_i)) \tag{24}$$

Thus, denoting $c_c = v_{\max}^2$, Lagrangian can be defined as

$$L(\boldsymbol{\Delta V}, \lambda) = \boldsymbol{\Delta V} \cdot (A_o + \lambda I) \cdot \boldsymbol{\Delta V} + 2\boldsymbol{b}_o \cdot \boldsymbol{\Delta V} + c_o - \lambda c_c \tag{25}$$

where $\lambda \geq 0$ is the Lagrange multiplier. In general, the QCQP with a single constraint can be expressed as semi-definite programming, whose solution is easily obtained by a convex optimization solver.[?] For the current problem, the solution to the dual problem can be semi-analytically obtained.

When there exists $\lambda \geq 0$ such that $A_o + \lambda I \geq 0$, which is the Slater condition, strong duality holds, and the dual function for the above Lagrangian is given as follows.[?]

$$g(\lambda) = \inf_{\boldsymbol{\Delta V}} L(\boldsymbol{\Delta V}, \lambda) = c_o - \lambda c_c - \boldsymbol{b}_o \cdot (A_o + \lambda I)^{\dagger} \cdot \boldsymbol{b}_o \tag{26}$$

where † indicates the pseudo-inverse. The solution to the primal problem is given by

$$\boldsymbol{\Delta V} = -(A_o + \lambda^* I)^\dagger \cdot \boldsymbol{b}_o \tag{27}$$

where λ^* is the solution to the dual problem.

$$\max_{\lambda} g(\lambda) \tag{28}$$

$$\text{subject to } \; A_o + \lambda I \geq 0 \text{ and } \lambda \geq 0 \tag{29}$$

Due to the reversibility of the dynamical system, a nonzero velocity change must result in a nonzero state variation; namely, $\boldsymbol{\delta v} \cdot A_o \cdot \boldsymbol{\delta v} > 0$ for any $\boldsymbol{\delta v} \neq \mathbf{0}$, which means $A_o > 0$. Thus, $A_o + \lambda I > 0$ holds true if $\lambda \geq 0$. Therefore, the dual function can be expressed as

$$g(\lambda) = c_o - \lambda c_c - \sum_{i}^{3} \frac{(\boldsymbol{b}_o \cdot \hat{\boldsymbol{u}}_i)^2}{\lambda + \lambda_i} \tag{30}$$

where λ_i and $\hat{\boldsymbol{u}}_i$ are the i-th eigenvalue and eigenvector of A_o. We note that $\lambda_i > 0$ and $c_c > 0$. Thus, the dual function has a unique global maximum for $\lambda \geq 0$. When $dg(\lambda)/d\lambda < 0$ at $\lambda = 0$, the solution to the dual problem is $\lambda^* = 0$. Otherwise, the solution is the root of $dg(\lambda)/d\lambda = 0$, which is obtained by a root-finding algorithm.

Simulation Setup

A nominal relative spacecraft formation reconfiguration use-case was developed in order to test the autonomous path planning algorithms and the method for analytical computation of impulsive TCMs. The initial state of the client RSO forming the reference orbit was expressed in absolute Cartesian ECI coordinates, denoted by ($^{\mathcal{N}}$), as shown in Table **??**. The corresponding initial and final (target) relative orbit states of the servicer spacecraft were expressed in relative Cartesian coordinates in the reference Hill frame, denoted by ($^{\mathcal{H}}$), as shown in Table **??**. The subscripts correspond to the initial formation at time $t_0 = 0$ and the targeted formation at time $t_f = +35,000$, or roughly $+6$ orbit periods from the epoch.

Table 1: Initial Absolute State Elements for the Client RSO

Osc. Qty.	Osc. Value	Osc. Qty.	Osc. Value	Mean Qty.	Mean Value
$^{\mathcal{N}}X_0$, m	-355,827.1151	$\widetilde{a}_0$, km	6963.9834	$\bar{a}_0$, km	6973.0583
$^{\mathcal{N}}Y_0$, m	-1,148,917.451	$\widetilde{\lambda}_0$, deg	83.454	$\bar{\lambda}_0$, deg	83.443
$^{\mathcal{N}}Z_0$, m	6,865,349.448	$\widetilde{i}_0$, deg	98.016	$\bar{i}_0$, deg	98.010
$^{\mathcal{N}}\dot{X}_0$, m/s	-4,539.244647	$\widetilde{q}_{10}$	5.577×10^{-3}	$\bar{q}_{10}$	5.850×10^{-3}
$^{\mathcal{N}}\dot{Y}_0$, m/s	5,989.806903	$\widetilde{q}_{20}$	-1.464×10^{-3}	$\bar{q}_{20}$	2.439×10^{-4}
$^{\mathcal{N}}\dot{Z}_0$, m/s	810.8943623	$\widetilde{\Omega}_0$, deg	306.285	$\bar{\Omega}_0$, deg	306.286

The full nonlinear transformations were applied to convert the relative servicer states to absolute ECI states and the absolute ECI states of both spacecraft to the corresponding osculating orbital elements. From there, the osculating orbital elements for both the client and servicer spacecraft were converted to mean orbital elements using the first-order approximate inverse of Equation (**??**), as described in the previous section on formation dynamics. Finally, the differential elements of the servicer at t_0 and t_f were computed as the arithmetic difference from the corresponding reference elements. The resulting absolute and differential orbital elements are included in Tables **??**−**??**. The initial formation is a safety ellipse (SE) with out-of-plane motion and an in-track separation between the servicer and client of approximately -800 m; the targeted formation is a walking safety ellipse (WSE) of smaller size that initially closes the in-track separation by approximately 300 m, but then drifts back in the negative in-track direction. The nominal formation reconfiguration use-case described here will be the basis for analysis throughout the remaining sections.

Table 2: Initial and Target Relative State Elements for the Servicer Spacecraft

Osc. Qty.	Osc. Value	Osc. Qty.	Osc. Value	Mean Qty.	Mean Value
${}^{\mathcal{H}}x_0$, m	-103.9746	$\delta\widetilde{a}_0$, m	0.131	$\delta\bar{a}_0$, m	0.238
${}^{\mathcal{H}}y_0$, m	-799.1326	$\delta\widetilde{\lambda}_0$, deg	-6.489×10^{-3}	$\delta\bar{\lambda}_0$, deg	-6.502×10^{-3}
${}^{\mathcal{H}}z_0$, m	3.5919	$\delta\widetilde{i}_0$, deg	1.143×10^{-4}	$\delta\bar{i}_0$, deg	1.144×10^{-4}
${}^{\mathcal{H}}\dot{x}_0$, m/s	0.0028341	$\delta\widetilde{q}_{10}$	1.740×10^{-6}	$\delta\bar{q}_{10}$	2.033×10^{-6}
${}^{\mathcal{H}}\dot{y}_0$, m/s	0.2206368	$\delta\widetilde{q}_{20}$	1.419×10^{-5}	$\delta\bar{q}_{20}$	1.415×10^{-5}
${}^{\mathcal{H}}\dot{z}_0$, m/s	0.1090468	$\delta\widetilde{\Omega}_0$, deg	8.270×10^{-4}	$\delta\bar{\Omega}_0$, deg	8.283×10^{-4}
${}^{\mathcal{H}}x_f$, m	-28.8750	$\delta\widetilde{a}_f$, m	24.910	$\delta\bar{a}_f$, m	25.417
${}^{\mathcal{H}}y_f$, m	-499.5620	$\delta\widetilde{\lambda}_f$, deg	-3.949×10^{-3}	$\delta\bar{\lambda}_f$, deg	-3.957×10^{-3}
${}^{\mathcal{H}}z_f$, m	-7.9990	$\delta\widetilde{i}_f$, deg	-1.347×10^{-4}	$\delta\bar{i}_f$, deg	-1.348×10^{-4}
${}^{\mathcal{H}}\dot{x}_f$, m/s	-0.0034510	$\delta\widetilde{q}_{1f}$	-1.325×10^{-6}	$\delta\bar{q}_{1f}$	-1.151×10^{-6}
${}^{\mathcal{H}}\dot{y}_f$, m/s	0.0728719	$\delta\widetilde{q}_{2f}$	7.224×10^{-6}	$\delta\bar{q}_{2f}$	7.295×10^{-6}
${}^{\mathcal{H}}\dot{z}_f$, m/s	0.0918294	$\delta\widetilde{\Omega}_f$, deg	6.941×10^{-4}	$\delta\bar{\Omega}_f$, deg	6.949×10^{-4}

RESULTS

Autonomous Path Planning

The reconfiguration described in the previous section and parameterized by Tables **??**–**??** was targeted using the risk-aware fuel-optimal path planning algorithms shown in Figure **??**. The end-to-end transfer is shown in Figure **??** where Figures **??** and **??** demonstrate the iterative refinement of the *n*-impulse fuel-optimal targeting solution. Following the logic of Figure **??**, the algorithm first solved a dense grid of maneuvers to achieve the final orbit (Figure **??**); the 11 impulse times were corresponding to the local maxima of the impulse history were selected as the candidate optimal times, and; the converged solution after the primer vector iteration process achieved the targeted formation reconfiguration with 4-maneuvers and a total ΔV of approximately 5.5 cm/s (Figure **??**).

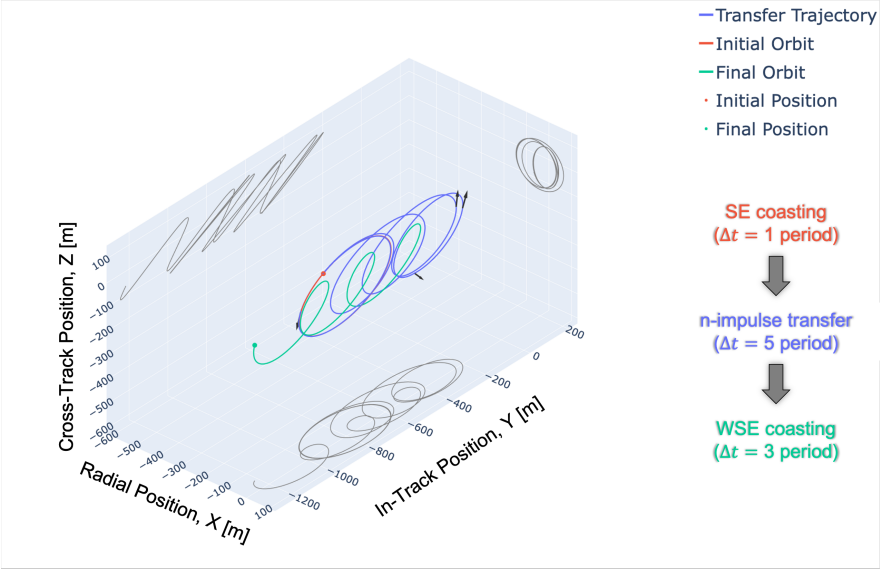

Figure 5: Nominal Use Case: Final Trajectory in the Hill Frame with the Client RSO Fixed at (0, 0, 0).

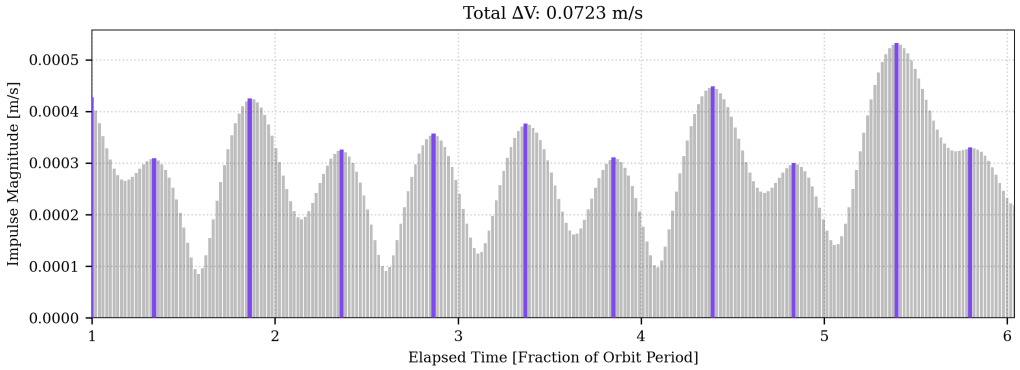

Figure 6: Nominal Use Case: Maneuver Magnitude History for Initial Energy Dense Solution with Candidate Optimal Maneuver Times Identified.

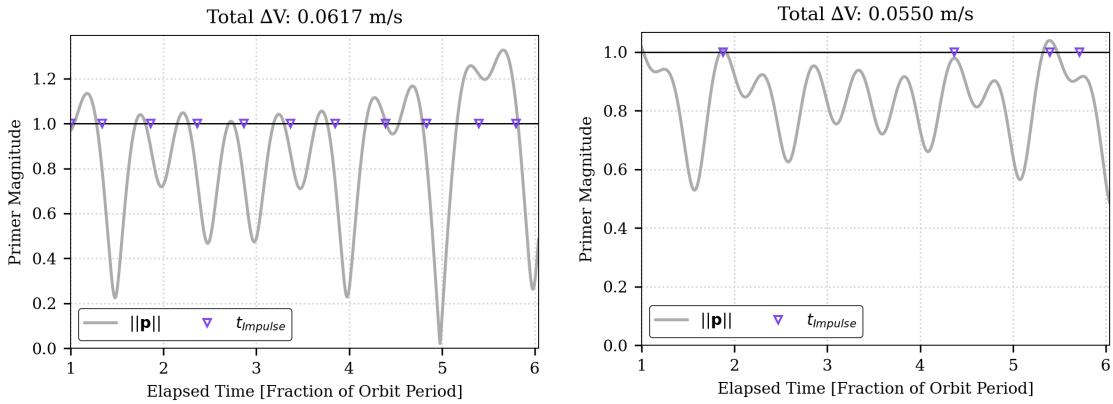

Initial Candidates

Near Optimal

Figure 7: Nominal Use Case: Primer Vector Magnitude History for Initial and Converged Maneuver Times.

Risk Analysis

The risk analysis is performed using the nominal trajectory and maneuver plan generated by the autonomous path planning algorithm in the previous section (Figure **??**). The behavior of the state uncertainties with different measurement sets and corresponding risk metrics is studied for the nominal trajectory.

As for the measurement update, the azimuth-elevation measurements and range measurements described earlier are used. Table **??** shows the noise parameters used for the covariance prediction for risk assessment. For the angle measurements, the uncertainty is assumed to be given by $\sigma = \text{IFOV}$ where IFOV is the pixel field of view of the optical imager. The current analysis assumes $\text{IFOV} = 60^\circ/500 \simeq 2.09$ mrad. The process noise covariance Q_i in Equation (**??**) is set to a constant diagonal matrix whose element is σ^2_{snc} and its value is determined by considering SRP and drag modeling errors. Namely, $\sigma^2_{\text{snc}} = \sigma^2_{\text{srp}} + \sigma^2_{\text{drag}}$, where $\sigma_{\text{srp}} = 6.840 \times 10^{-9}$ m/s and $\sigma_{\text{drag}} = 2.857 \times 10^{-15}$ m/s. These acceleration errors correspond to 20 percent of the nominal SRP and atmospheric drag, assuming the spacecraft's area-to-mass ratio of $(0.5)^2/50$ m^2/kg and atmospheric density of 10^{-13} kg/m^3. The measurement cadence is set to 5 minutes, which is a conservative assumption. Table **??** also lists the parameters for the Gates maneuver noise model in Equation (**??**). The initial covariance of the relative position and velocity in the Hill frame is set to a spherical covariance, where position and velocity uncertainties are 10 meters and 1 mm/s respectively.

Table 3: Parameters Used for Covariance Prediction.

Parameter	Value	Unit
σ_{optical}	2.09	mrad
σ_{range}	5.0	meter
σ_{snc}	6.84×10^{-9}	m/s
σ_s	0.01	-
σ_r	0.1	mm/s
σ_p	5.0	mrad
σ_a	0.1	mm/s

Figure **??** shows the predicted covariance without any measurement updates. There is notable growth in the in-track component of the position uncertainty, while uncertainties in other state elements have an oscillatory pattern. Figures **??** and **??** show the evolution of state covariance with only optical measurements and with optical and range measurements, respectively. With the optical measurement only, there is a relatively large range uncertainty as seen from the in-track position uncertainty, which is due to the scale invariance of the optical measurements. However, the range accuracy is less than 10 meters throughout the simulated trajectory. With the addition of direct range measurements, the uncertainty can be reduced to less than 2 meters.

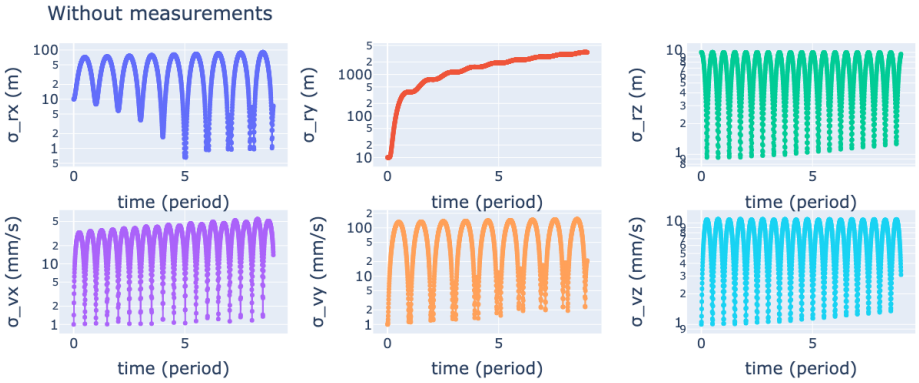

Figure 8: Time History of Predicted Relative State Covariance without any Measurements.

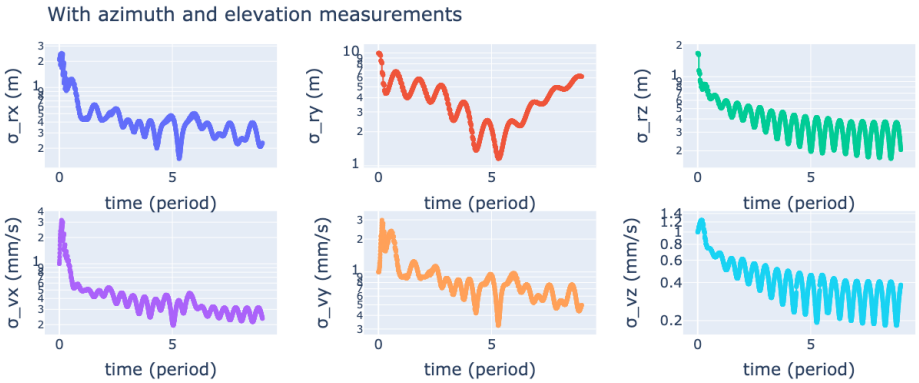

Figure 9: Time History of Predicted Relative State Covariance with Azimuth and Elevation Measurements.

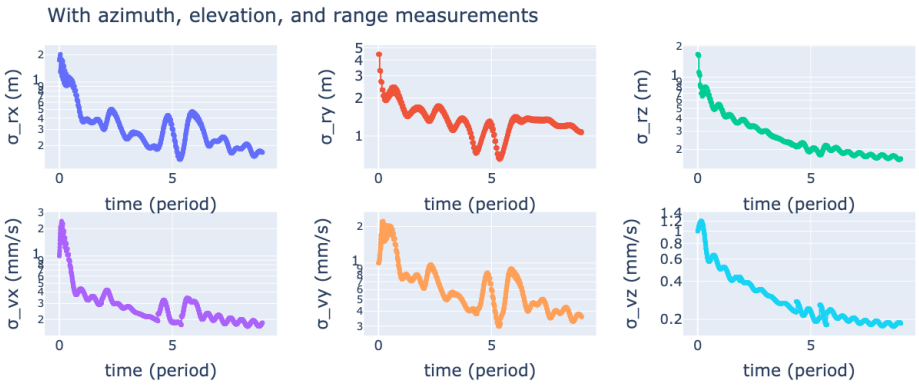

Figure 10: Time History of Predicted Relative State Covariance with Azimuth, Elevation, and Range Measurements.

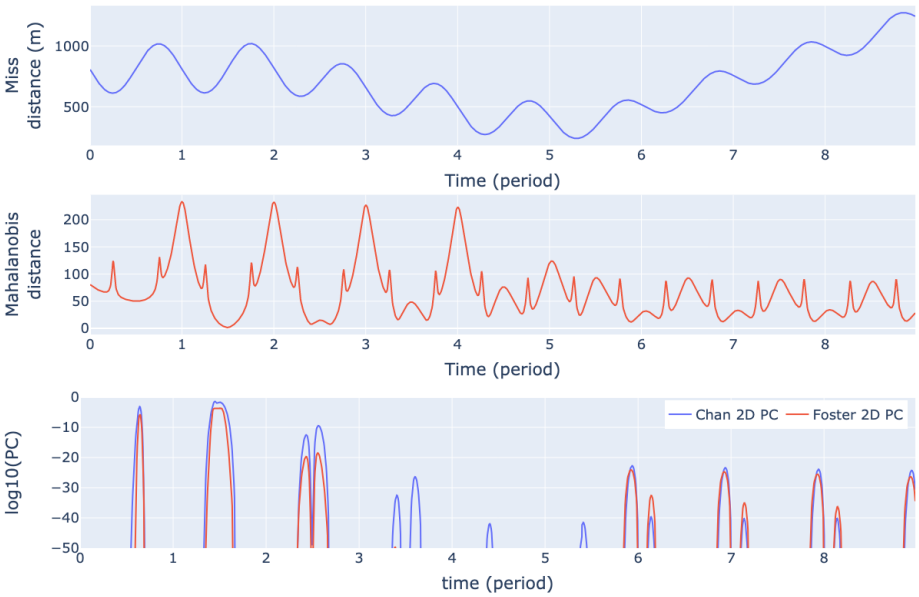

Figure 11: Time History of Miss Distance, Position Mahalanobis Distance, and 2D PC without Measurement Updates.

Figure **??** shows the time history of the miss distance, position Mahalanobis distance, and corresponding 2D PC when the covariance prediction is performed without assuming measurement updates. The minimum miss distance is around 240 meters at $t = 5.3$ periods. The minimum Mahalanobis distance is about 1.5 σ at $t = 1.5$ periods. An interesting observation is that the minimum Mahalanobis distance does not coincide with the minimum miss distance due to the highly elongated relative position covariance. The 2D PC plot shows the results of both Chan's and Foster's methods, and the two are in agreement. The maxima of the 2D PC correspond to the minima of the Mahalanobis distance. Thus, the Mahalanobis distance could be a useful measure for evaluating future risks and designing avoidance maneuvers. The maximum PC of $10^{-1.5}$ occurs at about $t = 1.5$ periods. Figure **??** shows the Mahalanobis distance history, along with miss distance history for reference when access to the optical measurements is assumed. The covariance for this case corresponds to Figure **??**. The Mahalanobis distance takes a minimum value at the beginning of the simulation and stays above 150 σ thereafter. The same observation regarding the minima of the miss and Mahalanobis distance holds as the case without measurement updates. The corresponding 2D PC is zero throughout the trajectory. The result indicates that even with a simple optical measurement, the state uncertainty becomes small enough,

resulting in a safe trajectory.

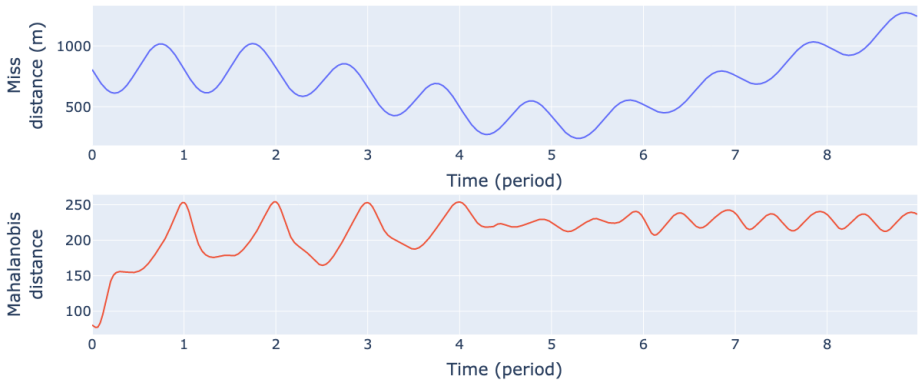

Figure 12: Time History of Miss and Position Mahalanobis Distance with Azimuth and Elevation Measurements. (2D PC is not shown as it is zero throughout the simulation, demonstrating the safety of the trajectory even with the conservative observation capability).

Formation Dynamics Errors

The full nominal trajectory, defined by the initial and target conditions of Tables **??**−**??** and the resulting maneuver plan was propagated using the full GA STM from Equation **??** and the effect of the impulses were accounted for with the GVEs (see Figure **??**). The corresponding ECI states were separately propagated via numerical integration of various force models in order to evaluate the accuracy of the GA-STM and quantify the error growth that can be expected due to the usage of a simplified dynamics model accounting only for the first-order J_2 secular perturbation.

The numerical integrator for this analysis was configured with the settings and Earth constants shown in Table **??**; the ballistic coefficients and solar radiation pressure (SRP) coefficients used for both the client and servicer spacecraft in this analysis are shown in Table **??**. The respective coefficients' differences characterize the differential drag and differential SRP effects and will drive the size of the discrepancy between the chosen analytical model and the numerical integration results including drag and SRP.

Table 4: Numerical Integrator Configuration and Earth Constants for Formation Dynamics Analysis.

Description	**Setting**	**Description**	**Setting**
Integrator:	Dormand-Prince 853	**Gravity Field Model:**	SGG-UGM-2
Min Step:	0.001 sec	$\boldsymbol{J_2 \equiv -\bar{C}_{20} \times \sqrt{5}}$**:**	0.0010826341979472214
Max Step:	1,000 sec	**Equatorial Radius:**	6,378,136.3 m
Rel. Tol.:	2×10^{-14}	**Gravitational Parameter:**	$3.986004415 \times 10^{14}$ m^3/s^2
Abs. Tol.:	4×10^{-10} m	**Atmosphere Model:**	NRLMSISE-00

Table 5: Spacecraft Model Parameters Used for Formation Dynamics Analysis

Description	**Setting**
Client $C_D \frac{A}{m}$	0.0235164 m^2/kg
Client $C_R \frac{A}{m}$	0.0150494 m^2/kg
Servicer $C_D \frac{A}{m}$	0.0227466 m^2/kg
Servicer $C_R \frac{A}{m}$	0.00621975 m^2/kg

While the full non-linear transformations were used to transform between absolute ECI states and corresponding orbital element representations for both the client and servicer spacecraft states to initialize the respective propagation methods, the full GA-STM in Equation (**??**) uses linearizations for both the mean↔ osculating transformation in addition to the transformation between differential orbital elements and the relative Hill frame Cartesian state. In order to asses the the error introduced by the latter linearization for the nominal use case, both propagation methods were compared using purely Keplerian motion (with $J_2 = 0$). The linearization causes an initial value error on the scale of 50 mm, largely in the radial component (Figure **??**). This is because the analytical propagation directly uses differential mean orbital elements and not the relative Cartesian state in the Hill frame.

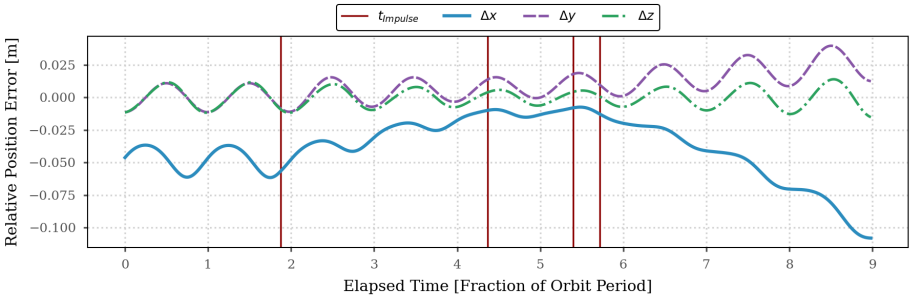

Figure 13: Analytical GA-STM vs Numerical Integration: Central Body ($J_2 = 0$)

Figure **??** shows a slightly larger error in the initial conditions, caused by the additional linearization effect of the mean to osculating transformation (with $J_2 \neq 0$). A secular growth in the in-track relative position error is also observed; this is caused by the GA-STM only accounting for first-order J_2 effects, and the in-track secular growth is of $\mathcal{O}(J_2^2)$. Finally, very small discontinuities are observed at each of the impulse times. This is caused by evaluating the GVEs on the reference orbit using the mean instead of the osculating orbital elements to save computational effort; the error is considered negligible for small accelerations.

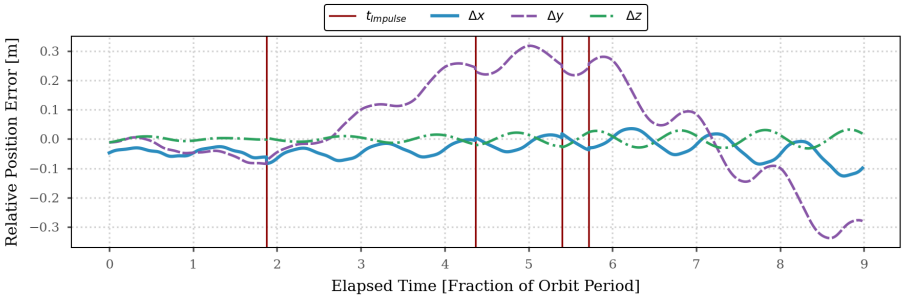

Figure 14: Analytical GA-STM vs Numerical Integration: Central Body + J2

Figures **??**, **??**, and **??** show the cumulative relative position error when comparing the GA-STM propagation to the numerical integration of the following force model configurations, respectively: a 70×70 Geopotential gravity field; the central body force + J_2 + atmospheric drag, and; the central body force + J_2 + SRP. These results confirm the expectation for differential drag to have the second largest perturbative effect on relative motion dynamics after J_2.

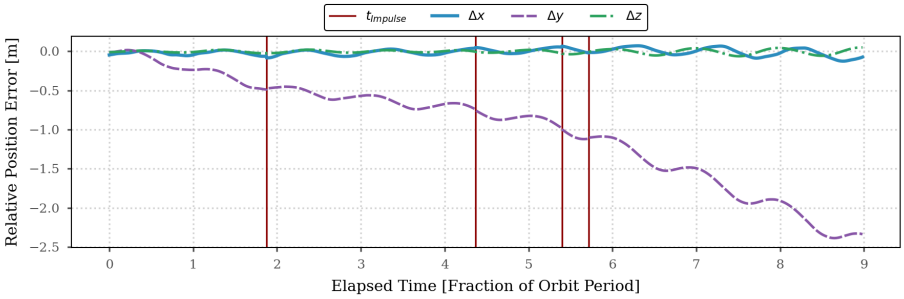

Figure 15: Analytical GA-STM vs Numerical Integration: Geopotential: 70x70

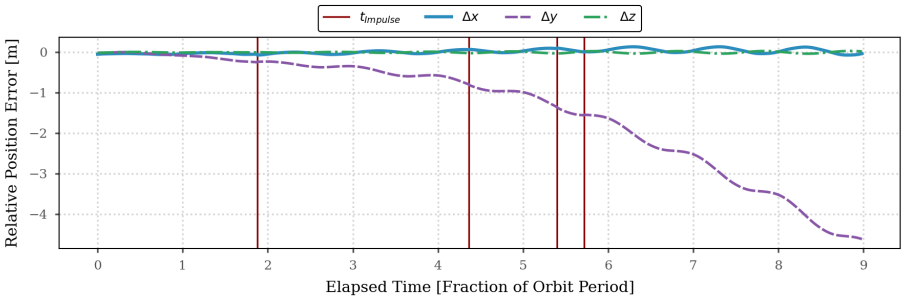

Figure 16: Analytical GA-STM vs Numerical Integration: Central Body + J2 + Drag

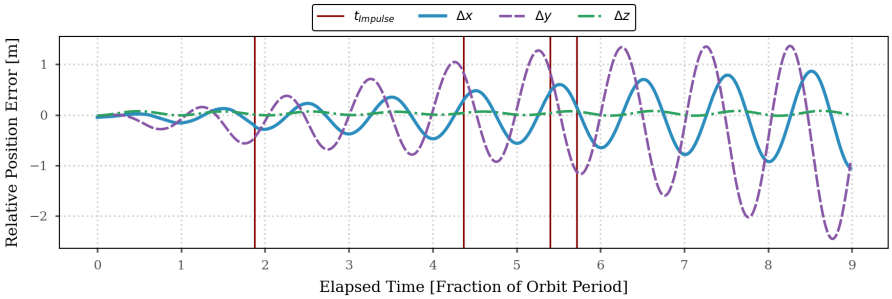

Figure 17: Analytical GA-STM vs Numerical Integration: Central Body + J2 + SRP

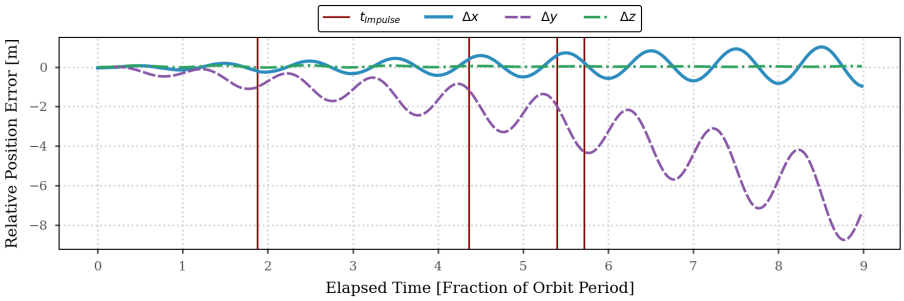

Figure 18: Analytical GA-STM vs Numerical Integration: Geopotential: 70x70 + Drag + SRP + Sun + Moon

Finally, Figure **??** shows a maximum 2-norm error of approximately 9 m when comparing the analytical GA-STM propagation to the numerical integration of a 70×70 Geopotential gravity field, atmospheric drag, SRP, and solar and lunar third-body effects. These results characterize the error that will be observed with respect to the nominal trajectory produced by the path planning algorithms using the GA-STM, and the following section demonstrates how the analytical QCQP approach can be used to efficiently compute TCMs onboard to address these errors.

QCQP-based TCM

The performance of the QCQP-based guidance law is presented here. The analysis uses the nominal trajectory defined earlier as a target trajectory, and the guidance law aims to minimize the future state deviation from the nominal trajectory. The initial state of the perturbed trajectory is shifted by $\boldsymbol{\delta\rho} = [1, 1, 1]$ m and $\boldsymbol{\delta\dot{\rho}} = [1, 1, 1]$ mm/s. The cost function of the QCQP in Equation **??** is used, and 10 target points $\boldsymbol{x}(t_i)$ are selected in 8 periods $\leq t_i \leq 9$ periods. The weight matrix is chosen to be

$$W = \begin{bmatrix} I_{3\text{x}3}/\sigma_\rho^2 & 0_{3\text{x}3} \\ 0_{3\text{x}3} & I_{3\text{x}3}/\sigma_{\dot{\rho}}^2 \end{bmatrix} \tag{31}$$

where $\sigma_\rho = 1$ m, $\sigma_{\dot{\rho}} = 1$ cm/s. Using this weight, the position deviation of σ_ρ and velocity deviation of $\sigma_{\dot{\rho}}$ are penalized equally. The maximum permissible $|\boldsymbol{\Delta V}|$ is set to 1 cm/s for the analyses shown here.

Figure **??** shows the result of applying the QCQP-based TCM at $t = 0$. The plot at the top shows nominal, perturbed, and corrected trajectories. The middle plot shows the time history of the state deviation from the nominal state for the cases with and without the TCM. The plot at the bottom shows the dual function and its first and second derivatives with respect to the Lagrange multiplier λ. The solution λ^* is indicated as a red marker. Without the TCM, the trajectory keeps drifting in the negative in-track direction. With the TCM, the position deviation can be bounded within ± 3 meters, and the trajectory looks identical to the nominal trajectory in the 3D plot. The dual function for this example case is maximized at $\lambda = 0$. Thus, the TCM does not require the maximum ΔV to minimize the cost function. Indeed, the ΔV for required this TCM is 3.49 mm/s. Figure **??** shows another example case where the maneuver is performed at $t = 6$ periods. The same plots are shown as the earlier example. For this case, the dual function takes a maximum value at $\lambda \neq 0$. Thus, the maximum ΔV constraint is active. The resulting TCM has a larger state deviation compared to the TCM performed at $t = 0$.

Figure **??** shows the optimal cost J and constraint $c(\Delta V) = \Delta V^2 - v_{\max}^2$ as a function of maneuver time. We can confirm that depending on the location of the maneuver, the optimal cost varies. Also, the cost increases as the maneuver time is delayed, which is intuitive as the trajectory keeps deviating from the reference and requires more control efforts. The trend of the constraint function shows that when the maneuver is performed early, maximum ΔV is not required to minimize the cost. Maneuvers performed later require larger ΔV, and after about $t = 5.5$ periods, the maximum ΔV constraint of 1 cm/s is reached.

Dispersion Analysis Result

While the risk analysis presented earlier demonstrates the safety of the nominal trajectory when basic optical measurements are available, it also shows a large covariance growth by natural dynamics. Therefore, if the spacecraft does not perform constant TCMs, the relative trajectory could be off by a significant amount from the nominal trajectory, which could result in higher risk. To further gain insight into the risk aspect, a dispersion analysis is performed by randomly sampling the initial relative state and maneuver execution errors. The analysis uses the same nominal trajectory introduced earlier.

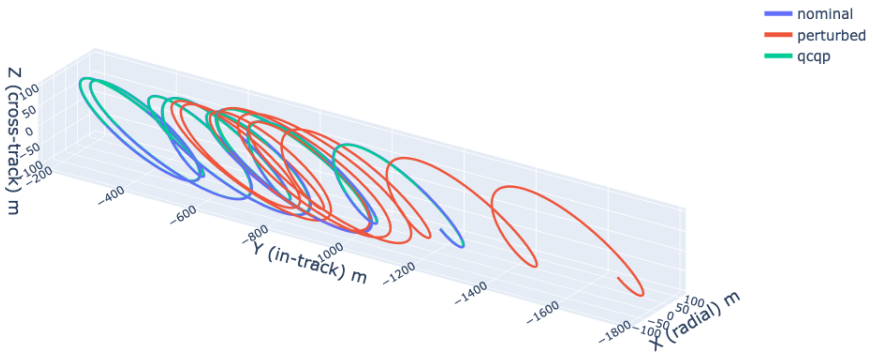

Trajectory (nominal, perturbed, and controlled).

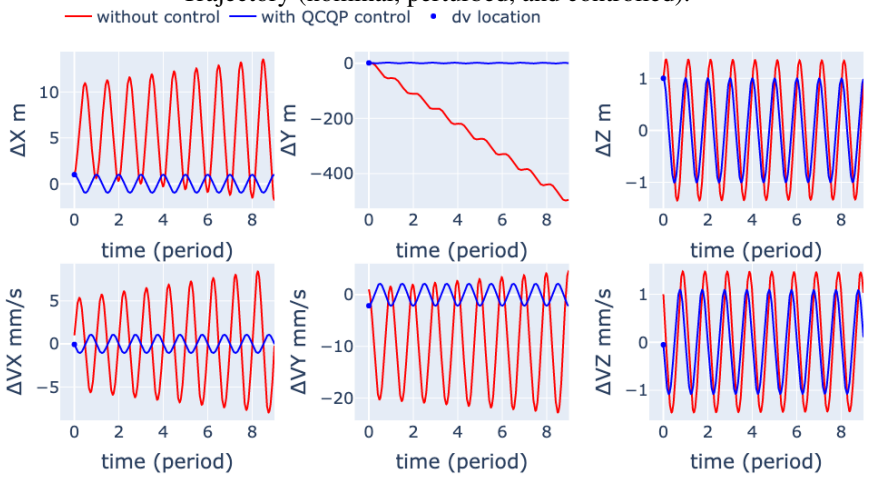

Time history of state deviation from the nominal.

Dual function and its derivatives.

Figure 19: Example Result of TCM Applied at t = 0 Peroods.

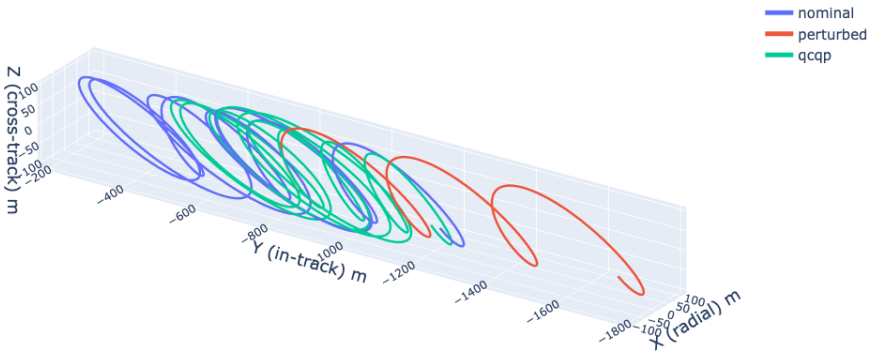

Trajectory (nominal, perturbed, and controlled).

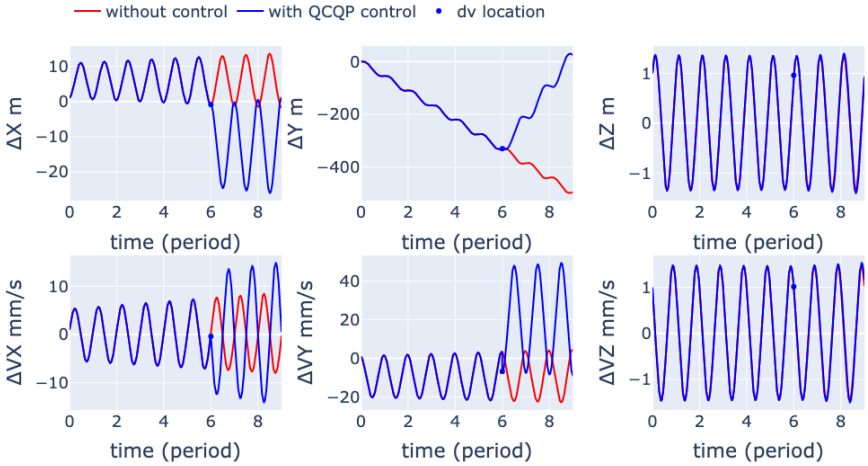

Time history of state deviation from the nominal.

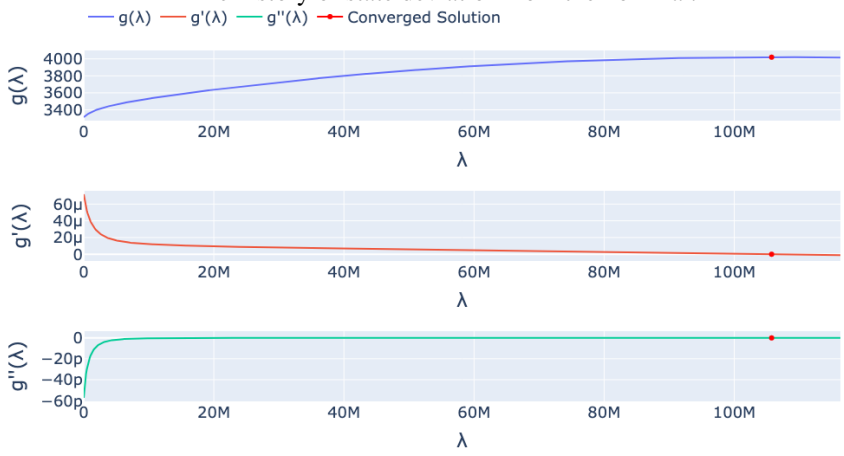

Dual function and its derivatives.

Figure 20: Example Result of TCM Applied at t = 6 Peroods.

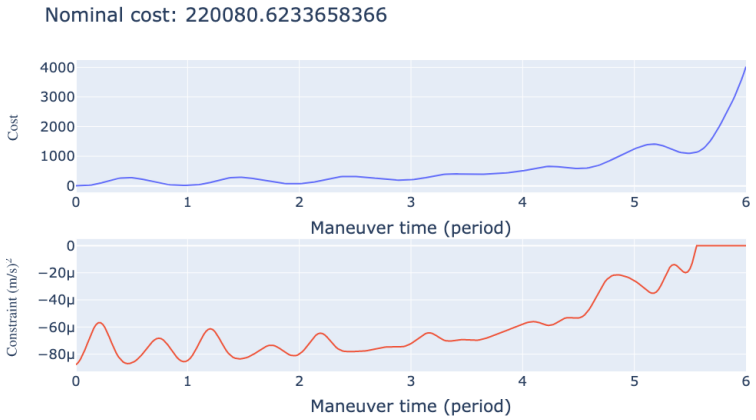

Figure 21: Cost and Constraint of QCQP-Based TCM as a Function of Maneuver Time.

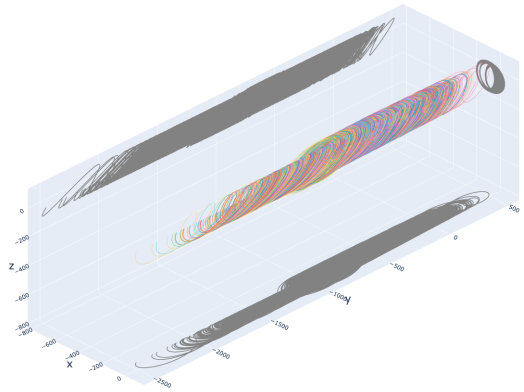

Figure 22: 3D plots of trajectories sampled in the Monte Carlo simulation.

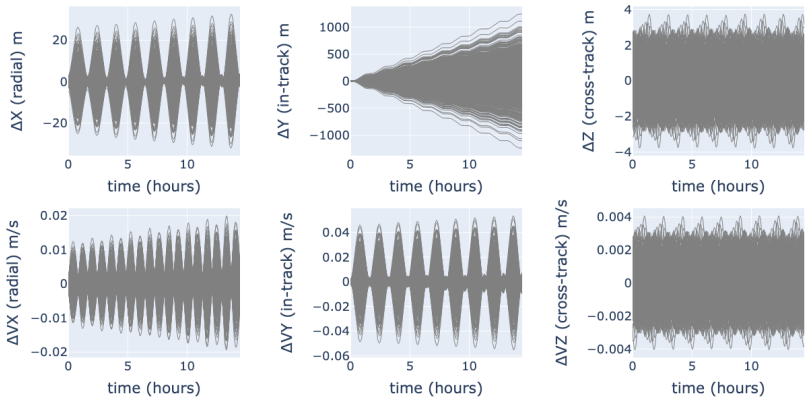

Figure 23: Time history of the state deviation from the nominal state generated from the Monte Carlo simulation.

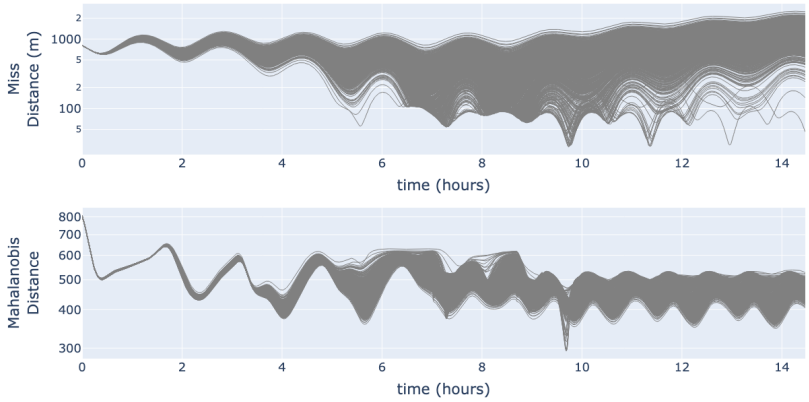

Figure 24: Time history of the risk metrics computed for each trajectory sampled in the Monte Carlo simulation.

Monte Carlo runs are performed 1000 times. In each run, the initial relative state in the Hill frame is sampled from a spherical Gaussian distribution with $\sigma_\rho = 10$ m and $\sigma_{\dot{\rho}} = 1$ mm/s. The maneuver execution errors are sampled using the Gates model with the same parameters shown in Table **??**. The maneuver execution error also includes a timing error of $\sigma = 1$ sec. For each sampled trajectory, the covariance prediction is performed by incorporating the azimuth and elevation angle measurements, process noise, and maneuver execution errors in the same way as the risk analysis shown earlier. The same parameters as shown in Table **??** are used for the covariance prediction. The measurement cadence is set to 60 seconds, which is reduced from the 5 minutes in the earlier analysis but is still a conservative assumption.

Figure **??** shows the 3D plot of trajectories sampled in the Monte Carlo simulation, and Fig. **??** shows the corresponding time history of the state deviation from the nominal state. As expected, we can confirm that there is a notable position drift in the in-track direction. Other state elements oscillate around the nominal states. Figure **??** shows the miss distance and Mahalanobis distance for these trajectories in log scale. The minimum miss distance of 28 meters occurs at around $t = 9.7$ periods. The corresponding Mahalanobis distance, which is also the minimum value is 293 σ, and the 2D PC is zero. Thus, the result still shows safety when basic relative measurements are available.

Astroscale 6-DOF Simulator

As a next step, we utilize the Astroscale high fidelity 6-DOF simulator to further analyze the trajectories. The purpose of this tool is to simulate various RPO maneuvers, generating the state of both servicer/client satellites in Semi-Non-Singular Keplerian (SNSK) or D'Amico Relative Orbital Elements, and covariance for both servicer and client satellites. Phases of the various RPO maneuvers considered in this study include safety ellipses towards the client; natural motion circumnavigation (NMC); and point of insertion (i.e., the point where the last maneuver occurs prior to entering an NMC for docking or the client's targeted pointing). This simulator includes a list of sensors to aid the guidance, navigation, and control for the various phases of the simulated maneuvers. Figure **??** shows the 6-DOF architecture.

The goal of this section is to analyze the RPO trajectory output of the Kayhan-provided maneuvers, both before and after the Proxima improvements, in the high-fidelity Astroscale simulator. The initial conditions shown in Table **??** are used for this case study as well. Based on these conditions, the IR-CAM is selected to provide measurements during the relative navigation towards the desired target. This sensor is capable of providing a relative position vector and attitude from 1 km to 250 m away from the client.

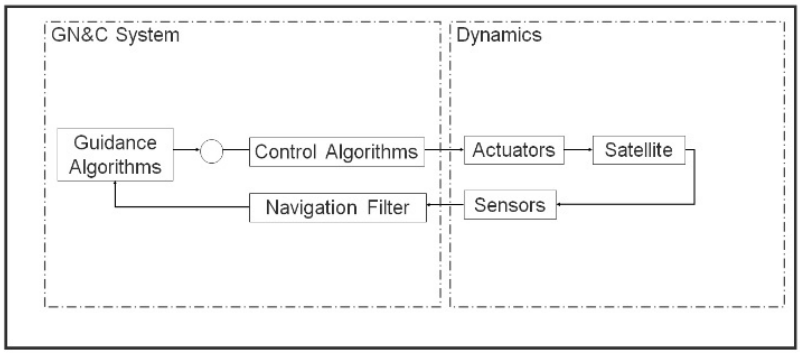

Figure 25: Architecture of the Astroscale 6-DOF Simulator

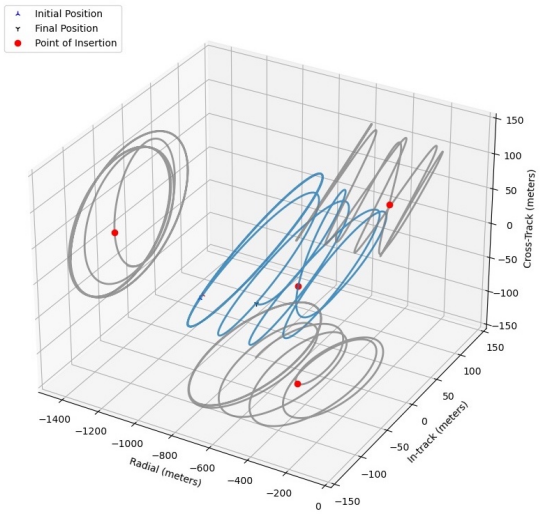

Figure 26: 3D Plot and 2D Projections of Trajectories Generated by Kayhan Proxima Algorithm.

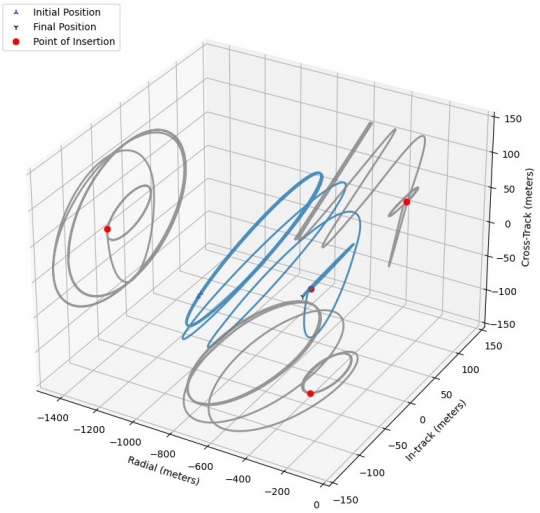

Figure 27: 3D Plot and 2D Projections of Trajectories Generated by 6-DOF Simulator with the 2x0 Gravity Model.

Given the initial condition and desired target in Tables **??** and **??**, the trajectories shown in Figures **??** and **??** were generated using the Kayhan Proxima algorithms and the 6-DOF simulator, respectively. We note that the 6-DOF simulator uses a different maneuver planning algorithm as described shortly, generating a different transfer trajectory. Also, it is worth mentioning that 6-DOF simulator results showed a noisy trajectory due to sensor noise. However, in terms of comparison, we only plot truth state data without the sensor measurements. Both the Kayhan Proxima algorithms and the 6-DOF simulator calculated 4 maneuvers to reach the point of insertion.

The 6-DOF simulator has high-fidelity capabilities. As a result, several uncertain parameters, such as the gravity model coefficients, sensor accuracy, and actuation output can be varied, which would have an impact in reaching a desired point in the trajectory. The perturbations due to J_2 and atmospheric drag have an impact on the total ΔV from applied fuel maneuvers. As the number of harmonic coefficients is increased in the gravity field, the total ΔV consumed increases. Atmospheric drag also plays a key role in the total ΔV consumption. In addition, the 6-DOF Simulator trajectories show that the servicer ends up further off target at the insertion time. The 6-DOF simulator accounts for realistic error biases and uncertainties that prevent the servicer controller from always reaching the target. A more detailed figure of the distance between the servicer and the point of insertion, while varying coefficients of the gravity field and capturing atmospheric drag, can be observed in Figure **??**.

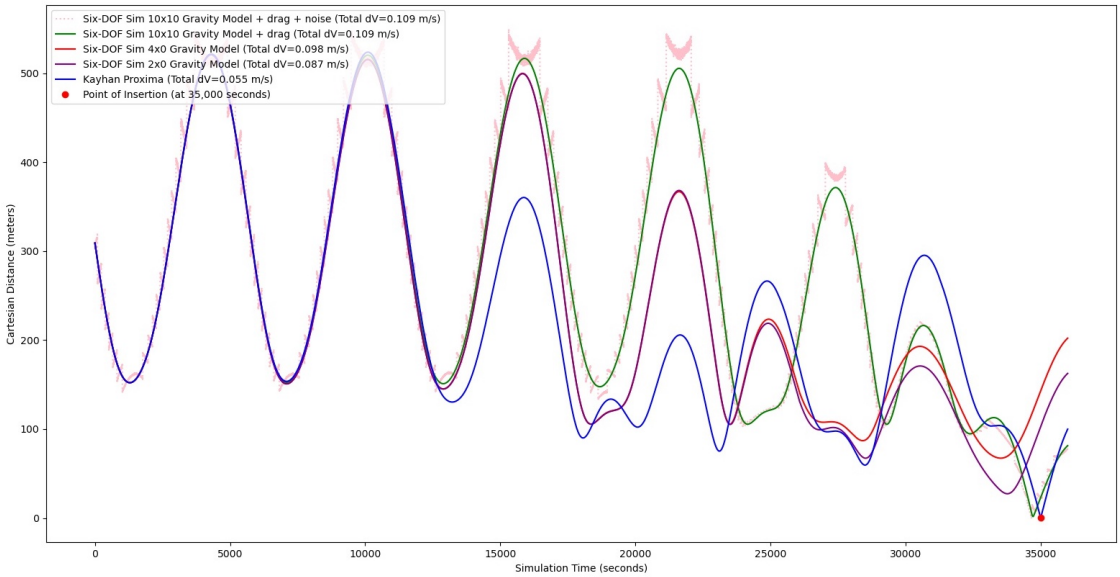

Figure 28: Time History of the Distance from the Insertion Point, Comparing Different Scenarios Generated from the 6-DOF Simulator and Kayhan Proxima.

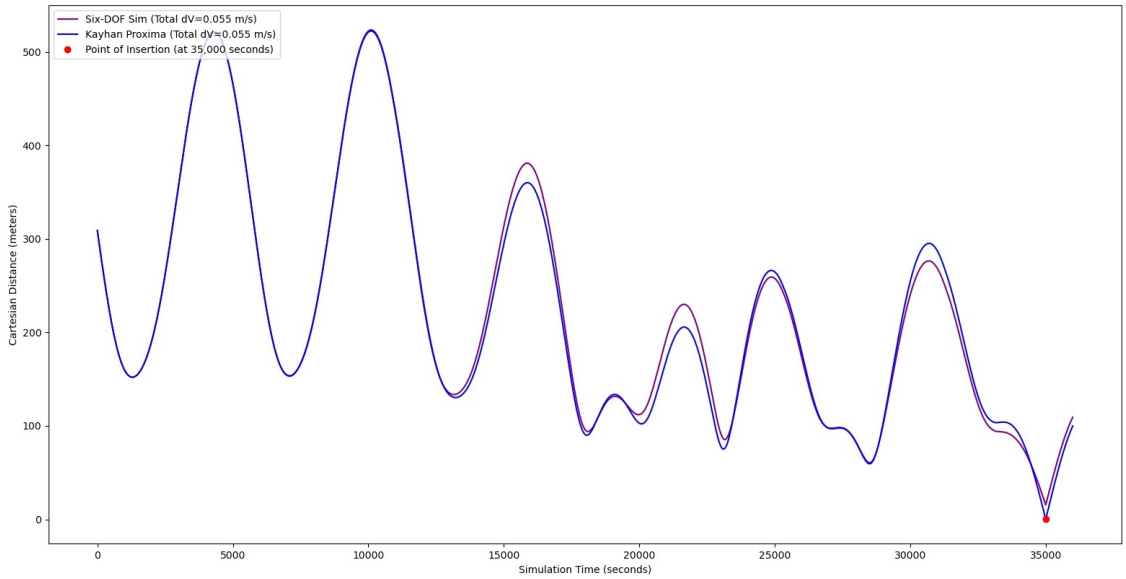

Figure 29: Time History of the Distance from the Insertion Point, Comparing the Result of Running the 6-DOF Simulation with the Kayha Proxima Maneuver Recommendation and the Nominal Trajectory Kayhan Proxima Targets.

The ΔV output of Kayhan Proxima algorithms is compared with the closest gravity model of the 6-DOF simulator. The 6-DOF simulator shows a higher total ΔV consumption of applied burns than Kayhan's Proxima algorithms. The main reason for this difference is the control technique of each approach. The 6-DOF simulator uses a control strategy from D'Amico,[?] which is conservative in nature and enforces the constraint of anti-parallelism of the eccentricity and inclination vectors of the servicer/client satellites. Kayhan's strategy minimizes the total ΔV maneuvers, and accounts for safety by forward-propagating the covariance and analyzing the predicted Mahalanobis distance and 2D PC versus time in the path planning algorithm. The

risk mitigation is also accounted for with their methods before a maneuver plan recommendation is executed.

Kayhan's ΔV recommendations are added to the 6-DOF simulator. The results show a similar servicer's state output and fuel usage as the nominal trajectory that Kayhan Proxima targets. Small errors represent the mismatch of the gravity field model and other approximation errors in computing the state transition matrix from Alfriend[?] such as first order J_2 approximation.

CONCLUSIONS AND FUTURE WORK

The concept of a zero-SWaP flight software enhancement that does not require a costly sensor suite or ADCS hardware additions is proposed and studied, with the goal of enabling safe and autonomous RPO and RPOD activities. In a conventional approach, the operations are highly manual and require intensive support from the ground stations for navigation and guidance. With autonomous GN&C capabilities, the cost and operational efforts can be reduced, enabling more efficient servicing. The system is under the influence of various uncertainties due to navigation errors, maneuver execution errors, and unmodeled dynamical errors. Therefore, autonomous servicer spacecraft needs to be cognizant of the risks that arise from such inherent errors and to have the capabilities to efficiently assess and mitigate the risks within the limited resources of onboard flight software.

The current work considers the analytical formulation of relative motion dynamics, using the GA-STM that can be applied to general elliptic client's orbits under the J_2 perturbation. Different representations of the relative state between the client and servicer spacecraft and transformations among them are explored to allow the proposed FSW enhancement to interface with the onboard software in a flexible manner. The risk-aware autonomous path planning algorithm is proposed that generates fuel-optimal maneuver commands while ensuring safety. The performance of the proposed control policy is demonstrated with numerical simulation. The risk analysis is then performed by predicting the relative covariance, and the result identifies key risk metrics such as position Mahalanobis distance. The risk analysis and subsequent dispersion analysis also confirm that the trajectory generated by the control policy is safe when accounting for optical bearing measurements, even with conservative measurement precision and collection cadence. The study also proposes an adaptive feedback control scheme using QCQP with a single constraint, which is known to be solvable in a polynomial time by converting to an equivalent convex optimization problem. In this study, a trajectory correction maneuver is formulated as a QCQP, and its analytical solution is directly derived. The control commands from the proposed autonomous path planning policy are also evaluated by Astroscale using a higher-fidelity 6-DOF simulator. The result confirms the proposed solution results in a fuel-efficient operation while achieving the required reconfiguration under the influence of unmodeled dynamical errors.

There are multiple areas that can be explored to further improve the performance and TRL of the proposed solution. Future work will address improving the fidelity of the analytical dynamical models, including the effects of other perturbations such as differential drag effects, differential SRP effects, higher-order gravity field effects, and higher-order contributions of J_2. Investigating accurate computation of the PC such as Monte Carlo PC or Hall 3D PC is also future work. The current analysis does not include avoidance maneuvers. We are planning to study an avoidance maneuver formulation in the QCQP or convex optimization framework for robust and efficient autonomous maneuver planning. Constraining the maneuvers to always ensure passive safety while still realizing fuel efficiency gains is of significant interest. As a result, trade studies between hardware/software failures and predictive covariance between servicer/client RSO will be performed to guarantee safety against uncertainty with our path planning algorithms. The work presented in this paper does not consider attitude motion, which needs to be addressed in the future. Also, the onboard relative navigation of the servicer spacecraft needs further analysis. As a path toward autonomous RPO demonstration, coordination and interfacing with the onboard G&NC system are necessary as well. The end-to-end simulation will be performed in the future, where the overall robustness of the system is tested, simulating truth states, measurement processing, navigation, and guidance in a closed loop, with FSW integration and validation and in-flight demonstration as the eventual target.

ACKNOWLEDGMENT

The authors extend their gratitude to AFRL and the US Space Force for their support of this research effort.